

## Article

# Constitutive Behavior and Mechanical Failure of Internal Configuration in Prismatic Lithium-Ion Batteries under Mechanical Loading

Zhijie Li <sup>1,2</sup>, Jiqing Chen <sup>1,2</sup>, Fengchong Lan <sup>1,2,\*</sup> and Yigang Li <sup>1,2</sup>

<sup>1</sup> School of Mechanical and Automotive Engineering, South China University of Technology, Guangzhou 510641, China; heaton\_lzj@163.com (Z.L.); chjq@scut.edu.cn (J.C.); lygcsu06@126.com (Y.L.)

<sup>2</sup> Guangdong Key Laboratory of Automotive Engineering, Guangzhou 510641, China

\* Correspondence: fclan@scut.edu.cn; Tel.: +86-020-87113955

**Abstract:** Internal short circuits and thermal runaway in lithium-ion batteries (LIBs) are mainly caused by deformation-induced failures in their internal components. Understanding the mechanisms of mechanical failure in the internal materials is of much importance for the design of LIB pack safety. In this work, the constitutive behaviors and deformation-induced failures of these component materials were tested and simulated. The stress-strain constitutive models of the anode/cathode and the separator under uniaxial tensile and compressive loads were proposed, and maximum tensile strain failure criteria were used to simulate the failure behaviors on these materials under the biaxial indentations. In order to understand the deformation failure mechanisms of ultrathin and multilayer materials within the prismatic cell, a mesoscale layer element model (LEM) with a separator-cathode-separator-anode structure was constructed. The deformation failure of LEM under spherical punches of different sizes was analyzed in detail, and the results were experimentally verified. Furthermore, the n-layer LEM stacked structure numerical model was constructed to calculate the progressive failure mechanisms of cathodes and anodes under punches. The results of test and simulation show the fracture failure of the cathodes under local indentation will trigger the failure of adjacent layers successively, and the internal short circuits are ultimately caused by separator failure owing to fractures and slips in the electrodes. The results improve the understanding of the failure behavior of the component materials in prismatic lithium-ion batteries, and provide some safety suggestions for the battery structure design in the future.

**Keywords:** lithium-ion batteries; component materials; constitutive behaviors; failure mechanisms; layer element model



**Citation:** Li, Z.; Chen, J.; Lan, F.; Li, Y. Constitutive Behavior and Mechanical Failure of Internal Configuration in Prismatic Lithium-Ion Batteries under Mechanical Loading. *Energies* **2021**, *14*, 1219. <https://doi.org/10.3390/en14051219>

Academic Editor:  
Giovanni Lutzenberger

Received: 12 January 2021  
Accepted: 18 February 2021  
Published: 24 February 2021

**Publisher's Note:** MDPI stays neutral with regard to jurisdictional claims in published maps and institutional affiliations.



**Copyright:** © 2021 by the authors. Licensee MDPI, Basel, Switzerland. This article is an open access article distributed under the terms and conditions of the Creative Commons Attribution (CC BY) license (<https://creativecommons.org/licenses/by/4.0/>).

## 1. Introduction

If an electric vehicle was involved in an accident or might run continuously on rough road surfaces, its lithium-ion batteries (LIBs) would be subjected to complex external mechanical loads, which could lead to some degree of deformation. A large deformation could damage the cell interior of the battery which induces short circuits or thermal runaway, while small deformations could cause small undetected internal cracks and fractures between the component material layers, which may potentially lead to micro-short circuits. According to the recent studies [1–3], different mechanical failure conditions of LIBs resulted in significantly different electrical-thermal responses, for example, Cannarella et al. [4,5] found that the LIBs manufactured with higher levels of stack pressure exhibited shorter cycle lives, because the higher levels of mechanical stress led to higher rates of chemical degradation, which affected the state of health (SOH) and state of charge (SOC) of the LIBs. Zhou et al. [6] established an electrochemical-mechanical coupling model with the consideration of the influence of elastic stiffening on diffusion for graphite anode materials. The results showed that during the normal charging and discharging of LIBs (such as static

without external mechanical loading), diffusion-induced stresses are generated which lead to deformation of electrode materials. Then, Zhou [7] developed a model for stresses generated during lithiation in the thin plate electrode considering the effects of external mechanical loading. The results showed that the external mechanical loading (negative stress gradient) enlarged stresses and deformation generated in the electrode materials, which led to the premature mechanical failure of LIBs after certain cycles. Wang [8] carried out uniaxial compression tests with different indentation depths on large format lithium-ion pouch cells. It was found that with the change of indentation depth, the internal short-circuit response of these cells shows different levels. The indented cells were disassembled and inspected for internal failure phenomenon, and observed multiple failure behaviors, including breaking of metallic current collectors (foils), shear slip of active coating materials, and rearrangement of fragments. Marcicki et al. [9] performed the impact experiments on cells with a rod which expressed a small drop ( $\Delta V = 200$  mV) in open-circuit voltage occurs the instant of the impact. Although the cell could normally continue to discharge after the impact, the temperature at the impact site had increased significantly, which indicated that the cell had a short circuit. These results show that the mode of internal deformation failure could significantly affect the short-circuit responses.

Many published literatures have reported the related research. For example, Finegan et al. [10] utilized a conical nail to puncture a LIB horizontally, middle along the cell, in which severe thermal runaway occurred though the component materials above the punctured region were not significantly deformed. Sahraei and Wierzbicki et al. [11,12] conducted comprehensive studies on how deformations and failures in a LIB during mechanical abuse lead to short circuits and thermal runaway; particularly, they deployed indenters of varying size and shape to conduct mechanical abuse experiments on lithium-ion pouch cells and cylindrical cells. Greve et al. [13] performed radial crushing, local lateral indentation, and global three-point bending tests on cylindrical LIBs. It was found that local indentation resulted in deformation failures and internal short circuits in the component materials at the contact zone and three-point bending led to tensile fractures and internal short circuits at the opposite side of the jellyroll, while radial crushing, on the other hand, did not form internal short circuits. These series of experimental studies have revealed that the failure mode is a significant factor for the short-circuit response of a LIB. Wang et al. [14] performed dual spherical indentation experiments on lithium-ion prismatic cells and exploited optical microscopy to observe the mode of failure of the battery's component materials. They observed multilayered shear cracks, fractures in the current collectors, and shear offsets in the coatings of the electrodes. Chung et al. [15] dissected the lithium-ion pouch cells that failed after local indentation and found that shear faults had fully sliced through the cell's internal layers. The internal failure of LIB is an instantaneous propagation from local damage to overall fracture. The fracture failure of internal component materials cannot be directly identified from macroscopic response curves (force, voltage, and temperature), because this phenomenon will be formed in mesoscopic displacement increment. Therefore, it is necessary to fully understand the mechanical properties and failure behavior of internal component materials.

The cell interior consists of unique multilayered porous structures. The active coating materials are compressible and possess complex plastic flow properties, while the metallic current collectors are tough and ductile. Furthermore, the separator is strongly anisotropic [16,17]. The tensile and compressive properties of the electrodes are significantly different, as their tensile strength depends on that of the current collector, while their compressive strength depends on the compaction and hardness of the active coating [17–20]. The current collector is more likely to cause fracture failure than coating, because the toughness of the current collector is lower due to the damage applied by a rolling process, and the failure occurs earlier than the same thickness of the non-damage current collector. The mechanical properties of the separator depend on its material makeup as well as the manufacturing process, since different manufacturing processes can lead to significant differences in the separator's mechanical properties. Based on multidirec-

tional mechanical tests on different types of separators, Zhang et al. [21] found that the dry-processed separators exhibit a greater degree of anisotropy than the wet-processed those. There are two distinct failure modes of dry-processed separators under different sizes of punches, which could explain the local micro-short characteristics of LIB. It was found that the tensile failure strain of the cathode/anode was far lower than that of the separator, thereby implying that internal short circuits within a LIB were primarily caused by the mechanical failure of the cathodes/anodes. A thoroughly understanding of the failure modes and sequences of component materials under mechanical loads is helpful to develop the finite element model of the layered structure.

A few researchers have studied the effects of mechanical abuse on LIBs using numerical and physical models. For example, Sahraei et al. [11,22] used a crushable foam material to model the homogenized behavior of small lithium-ion pouch cells aiming to predict the force-displacement relationship and moment of short-circuit formation under local indentation loading. Subsequently, a homogenized model for 18,650 cylindrical cells (whose mechanical properties were calibrated through a test) was developed to simulate the deformation and failure of these cells under various loads [12]. Wierzbicki et al. [23] proposed a method for modeling 18,650 cylindrical lithium-ion cells based on representative volume elements (RVEs), which allows the stress-strain relationship of cells under local indentation to be obtained by analyzing the mechanical properties of the RVE. These model-based approaches are capable of predicting the mechanical behaviors of LIBs under mechanical loads, but unable to characterize their internal failure modes accurately. Zhu et al. [24] constructed a model of lithium-ion pouch cells including the cathode coating, cathode collector, anode coating, anode collector, and separator layers, which can be used to predict the macroscopic mechanical responses of these cells and characterize their mesoscopic fracture failure modes accurately. Therefore, the layered structure model can reasonably describe the failure modes of the internal cell through the deformation failure of component materials. This type of refined modeling is important for understanding the mechanisms of mechanical failure in LIBs.

As compared to the other two types of cells, the prismatic cell has the same internal microstructure but with same differences in mechanical structure. For instance, the mechanical properties and thickness of the shell of the prismatic cell are orders of magnitude different from the internal component materials, which means that the electrodes are in a rigid constraint. When the electrodes expand within a constrained environment, the evolution of diffusion-induced stresses in prismatic cell is more complicated. In addition, it is more difficult to observe the internal failure of the prismatic cell under such protection of the shell. In the aspect of modeling, in order to understand the mechanical behavior of the ultrathin layered structure model and the influence of different material models to characterize the separator, a layer element model (LEM) was proposed, which was composed of separator, cathode, separator, and anode stacked alternately.

In this work, a series of mechanical tests were carried out in order to understand the mechanical properties and failure behaviors on internal component materials within prismatic cells, including uniaxial and biaxial tests on the cathode, anode, and separator. To understand the failure mechanisms of the cell interior under local indentation, a microscale LEM was constructed. By the combination of experiment and simulation, the deformation failure of current collectors, coating materials, and separators in the LEM under spherical punches were analyzed in detail. The analysis with LEM was effective and accurate for predicting the force-displacement relationship and fracture mode. Furthermore, the layered structure model of the n-layer LEM stacked was constructed, and the progressive failure mechanisms of cathodes and anodes under spherical punch were studied.

## 2. Materials and Methods

### 2.1. Structural Dimensions and Component Materials of Prismatic Cells

The prismatic cell was used. Dimension of this cell is 130 mm (length)  $\times$  65 mm (width)  $\times$  16 mm (thickness), and voltage/capacity is 3.2 V/10 Ah, as shown in Figure 1a. This cell

is composed of shell, interior, and electrolyte. The interior includes cathodes, anodes, and separators. The outside layer of the interior is wrapped by a layer of separator. The cathode and anode were prepared by coating both sides of the metallic current collector with active materials and rolling afterward. The cathode collector and the anode collector were made from aluminum foil and copper foil, respectively. The separators were ceramic-coated polymer films, as shown in Figure 1b. All the geometrical parameters of the prismatic cell are summarized in Table 1.



**Figure 1.** The photos of lithium-ion prismatic cells and internal component materials: (a) Prismatic shell and interior; (b) Internal component materials.

**Table 1.** Specifications of the prismatic cells and internal components.

Component	Material	Thickness ( $\mu\text{m}$ )
Prismatic shell	Aluminum	500
Cathode active layer (2 side)	LiFePO <sub>4</sub>	139
Cathode current collector	Aluminum	24
Anode active layer (2 side)	Graphite	85
Anode current collector	Copper	11
Separator	Alumina/PP/Alumina	20
Electrolyte	Ethylene Carbonate (EC)	-

## 2.2. Experimental Tests

### 2.2.1. Uniaxial Tensile Tests

Firstly, we performed uniaxial tests with the experimental specimens being prepared according to the ASTM D882 standard. Each specimen was cut into  $100 \times 10$  mm strips using a scalpel, and the gauge length was 50 mm, as shown in Figure 2a. Because the separator is anisotropic, the separator specimens were cut in the machine direction (MD,  $0^\circ$ ), diagonal direction (DD,  $45^\circ$ ), and transverse direction (TD,  $90^\circ$ ). An Instron uniaxial tensile tester with a maximum load of 2 kN was adopted as the tensile tester, the setup is shown in Figure 2b. To ensure that the ends of the specimen would be fully immobile and protected from clamping-induced damage during tensile testing, both ends of each specimen were protected with soft rubber, as shown in Figure 2c. The stretching speeds of the cathode/anode sheet and separator were 0.2 and 6 mm/min, respectively. The tensile tests were performed in triplicate for each set of specimens.

The stress-strain curves of the cathode, anode, and separator specimens to uniaxial tension are demonstrated in Figure 2d–f. These results indicate that the triplicate test curves of the cathode and anode specimens are highly consistent. The uniaxial stress intensity of the separator is much higher in the MD than in the DD and TD, with the stress intensity in the DD being similar to that in the TD, as shown in Figure 2f. The uniaxial tensile

failure strains of the separator in the MD and TD were approximately 0.7 and 1.4 in the DD, respectively. It may be observed that the triplicate test curves are highly consistent in all the three directions.

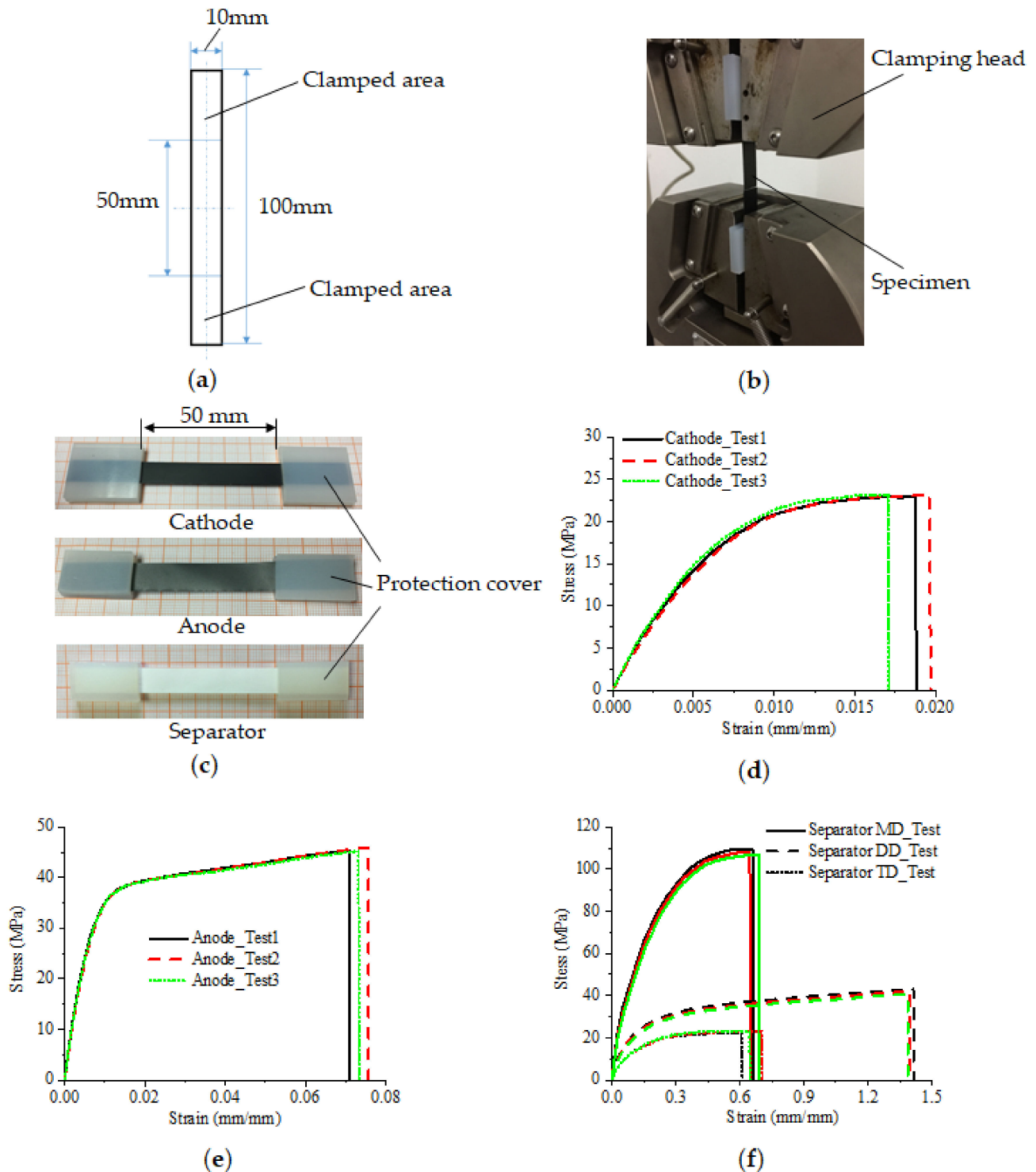


**Figure 2.** Tensile test of component materials of prismatic cell: (a) Specimen size; (b) Test setup; (c) Specimens of tested component materials; (d) Tensile stress-strain curves for cathode specimen; (e) Tensile stress-strain curves for anode specimen; (f) Tensile stress-strain curves for separator specimen.

### 2.2.2. Uniaxial Compressive Tests

Since the current collectors are isotropic materials, their tensile stress-strain curves could be used to characterize their compressive behaviors. However, the active coatings and separators are anisotropic materials and have distinctly different mechanical properties under tensile and compressive loads. The SUNS uniaxial compression tester with a maximum load of 100 kN was used to perform flat compression tests on the anode/cathode sheets and separator. The circular specimens of the 20-layer electrode stacked and 40-layer separator stacked were prepared using a  $\Phi 16$  mm punching tool. This ensured that all the specimens had the same shape and initial orientation, as shown in Figure 3a. Prior to the compression tests, the specimens were preloaded with 0.05 MPa of prestress to eliminate inter-specimen gaps. The compression speeds of the cathode/anode sheets and separators were 0.1 and 0.12 mm/min, respectively. The same strain rate was used in the compression tests and tensile tests, and the tests on each set of specimens were performed in triplicate. The stress-strain curves of the cathode, anode, and separator under uniaxial compression are demonstrated in Figure 3b–d. It can be observed that the compressive test curves of the component materials are consistent.

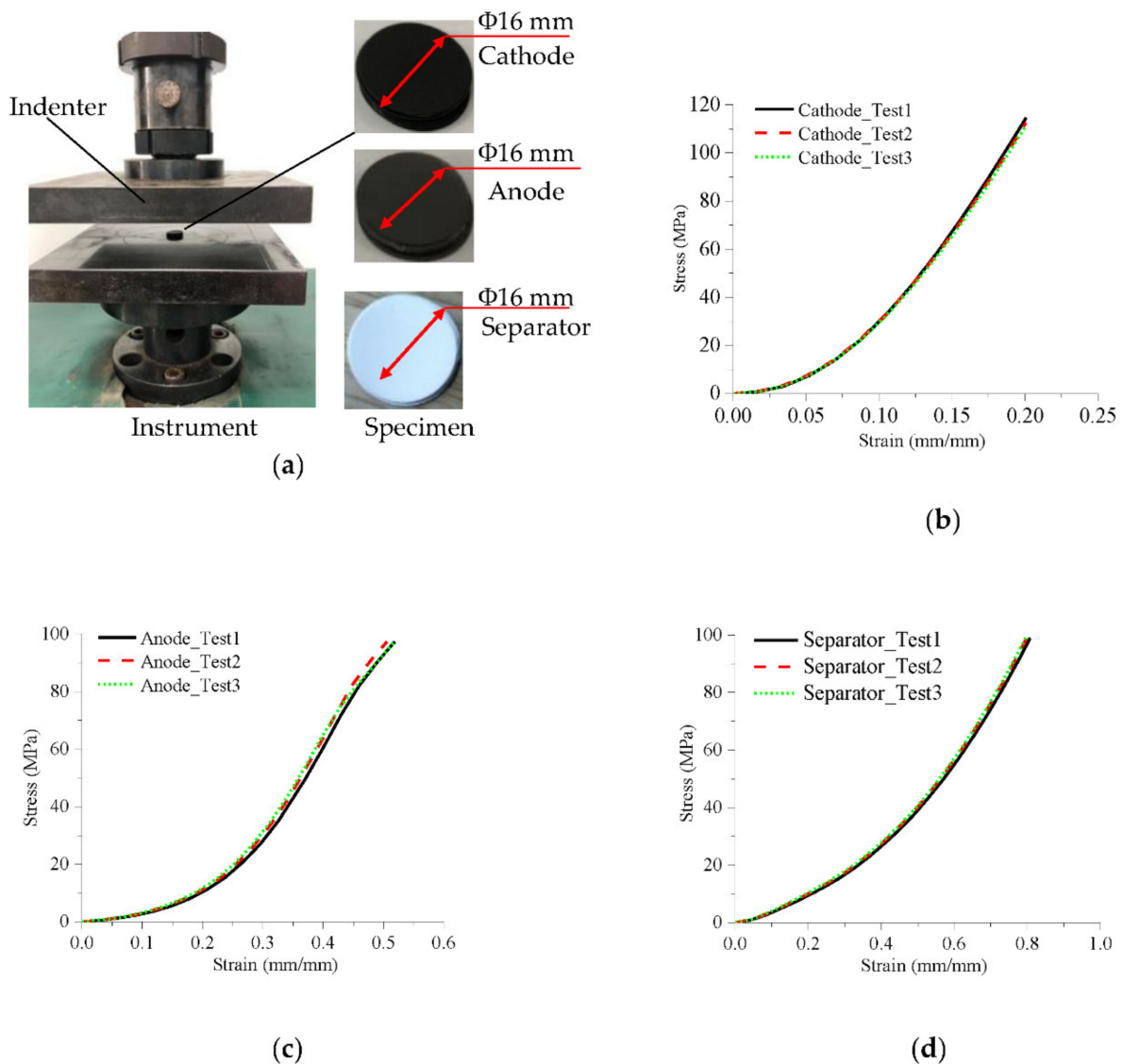


**Figure 3.** Compressive test of component materials for prismatic cell: (a) Test setup and specimens of tested component materials; (b) Compressive stress-strain curves for cathode specimen; (c) Compressive stress-strain curves for anode specimen; (d) Compressive stress-strain curves for separator specimen.

### 2.2.3. Biaxial Tests

A punch tool was used to cut the anode/cathode sheets into circular specimens. Subsequently, the specimens were affixed to a fixture consisting of a base, cappers, washers, and locking bolts, as shown in Figure 4a. The internal diameter of the clamp was 32 mm, and the washers were made of soft rubber, which immobilized the specimens and prevented specimen damage during the clamping process. An Instron compression tester with a maximum load of 5 kN was used in these tests. The biaxial loading were performed with spherical punches made out of Teflon (PTFE) to reduce friction coefficient, which is helpful to minimize friction-induced damage on the specimens' surfaces. The dimensions of the punches ranged from  $\Phi 6.3$  to  $\Phi 25$  mm, as shown in Figure 4b. The loading speed was 0.1 mm/min. The specimens would be subjected to the in-plane tension and out-of-plane compression during biaxial test (see Figure 4c,d). Figure 5 shows the force-displacement curves of the component materials under the  $\Phi 12.5$  and  $\Phi 6.3$  mm spherical punches. The fluctuation of the triplicate test curves of the cathode is more obvious than that of the anode and separator, which is caused by the slight shedding of the coatings during indentation.

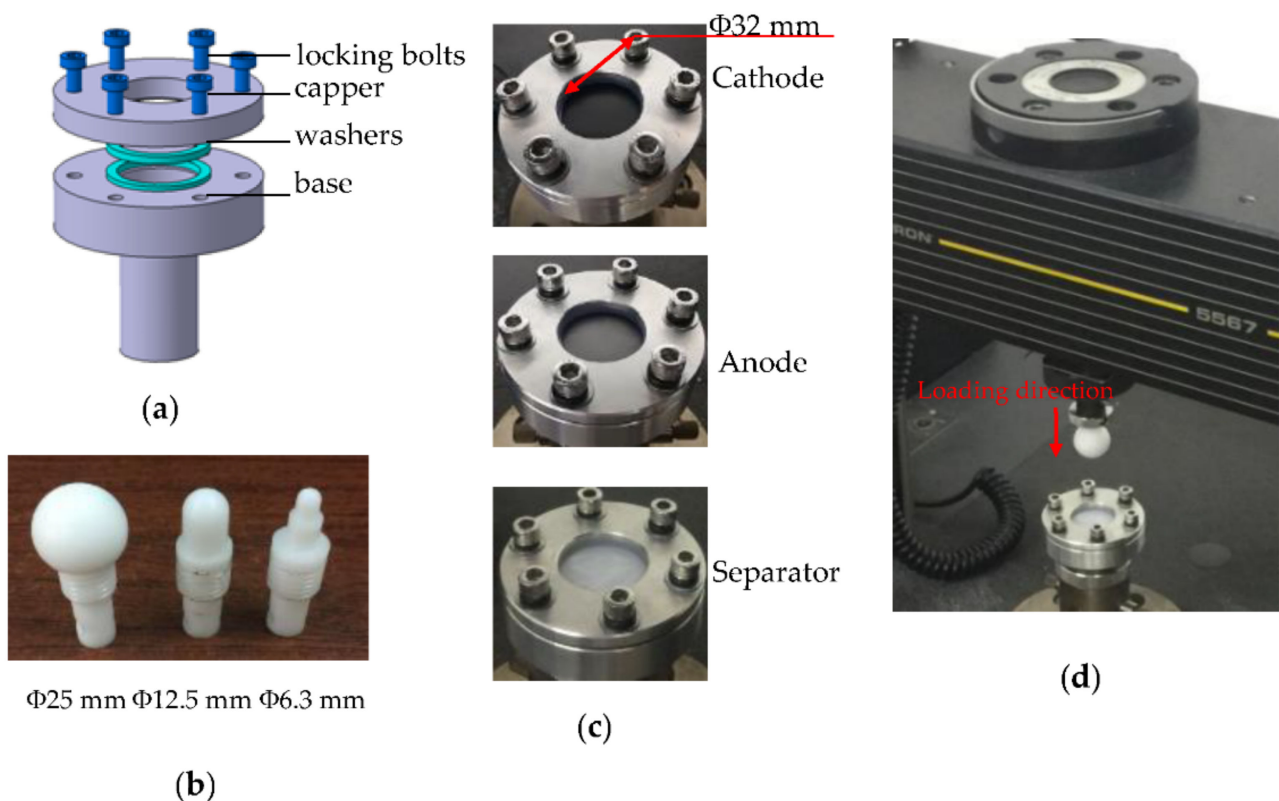


**Figure 4.** Biaxial experimental setup and test specimens: (a) Fixture; (b) Spherical punches; (c) Biaxial test specimens; (d) Biaxial experimental setup.

Since the mesoscopic deformations and failures in the internal component materials of the prismatic cell have a direct influence on the LIB's macroscopic mechanical responses, an in-depth study of their failure characteristics can enhance the accurate understanding of the mechanisms by which internal short circuits occur in LIBs. By performing a comprehensive series of mechanical tests on the anode, cathode, and separator, we can gain the insight into the mechanical behaviors and failure mode of these materials under a variety of loads, which provides support for the construction of accurate finite element models for the prismatic cell.

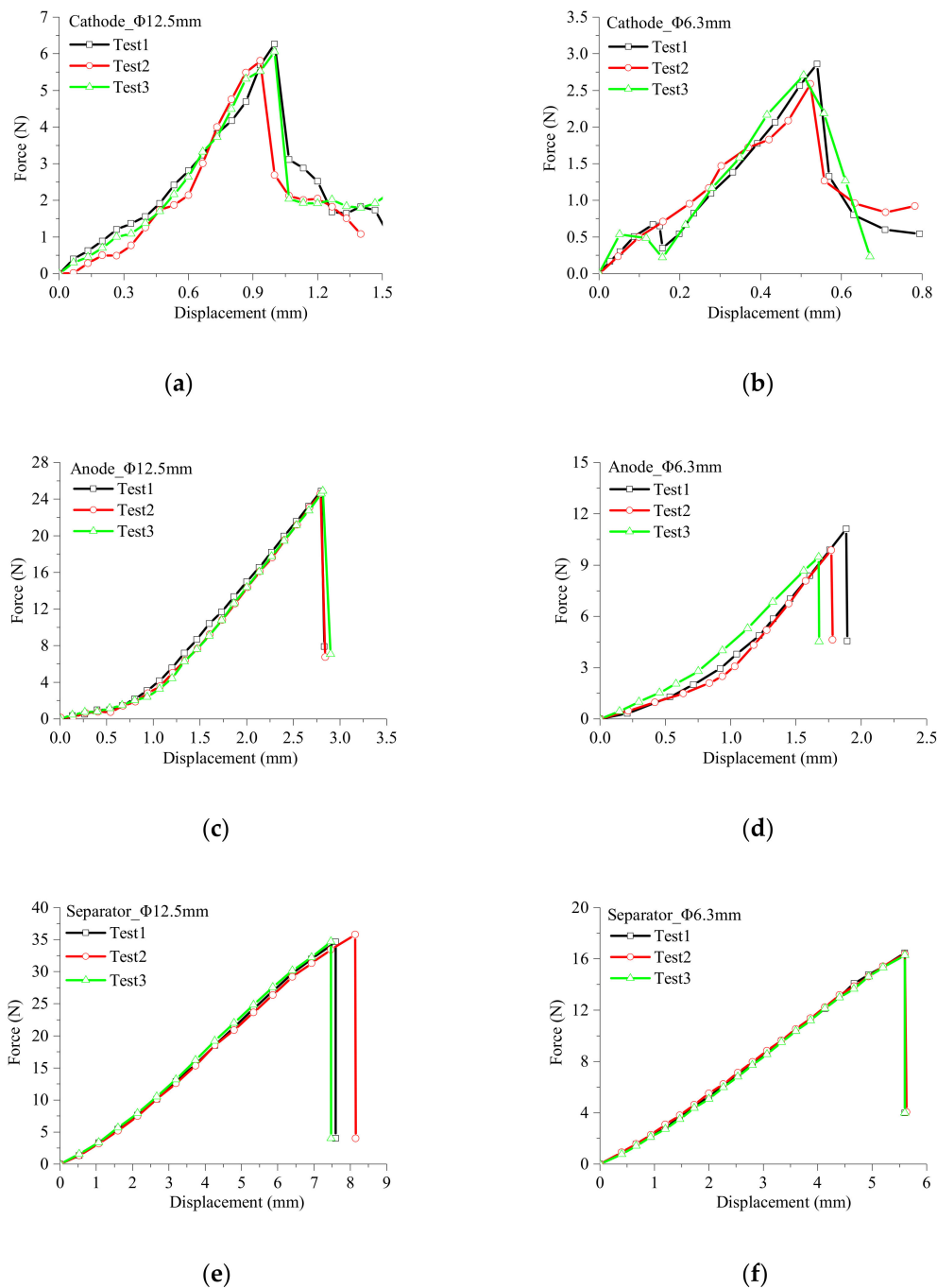


**Figure 5.** Force-displacement curves of lithium-ion prismatic cell components under different sizes of spherical punches: (a) Cathode tests under  $\Phi 12.5$  mm; (b) Cathode tests under  $\Phi 6.3$  mm; (c) Anode tests under  $\Phi 12.5$  mm; (d) Anode tests under  $\Phi 6.3$  mm; (e) Separator tests under  $\Phi 12.5$  mm; (f) Separator tests under  $\Phi 6.3$  mm.

### 3. Constitutive Properties of Component Materials and Modeling

The constitutive relationship of component materials in LIBs is the basis of constructing discrete layered structure model. The previous section gives a preliminary description of the uniaxial and biaxial tests of the electrodes and separators. In this section, the test results would be used to analyze the failure behaviors of component materials under different loads, and the corresponding constitutive relationship would be obtained. According to the constitutive properties, the finite element model of each component material is constructed.



### 3.1. Uniaxial Tension Properties

The active coatings on either side of the electrodes are porous composite materials that consist of a solid powder and polymer binder. Owing to the discontinuous nature of the coatings' porous structure, the current collector carries most of the load when the electrode is subjected to uniaxial tension. In the experiments of Wang et al. [25], it was observed that the electrode coatings were still intact even after the current collectors cracked, which implies that the former is more resilient than the latter. Furthermore, Sahraei et al. [19] also observed that the current collectors are more susceptible to cracks than the coating since the current collectors were damaged by the rolling that occurred during electrode fabrication. As a result, the uniaxial tensile failure strains of the anode/cathode specimens are similar to those of the current collectors. Assuming that the uniaxial tensile strains of electrodes, active coatings, and current collectors are equal under uniaxial tensile load, the following results can be obtained:

$$\varepsilon_e = \varepsilon_a = \varepsilon_c. \quad (1)$$

According to the tensile stress-strain curves, the electrodes characterized the elastic-plastic tensile behavior obviously, and the brittle fracture occurred. Therefore, the current collector was modeled using the isotropic linear-hardening model, and the expression was as follows:

$$\sigma = \begin{cases} E\varepsilon & \sigma < \sigma_s \\ \sigma_s + E_t(\varepsilon - \frac{\sigma_s}{E}) & \sigma \geq \sigma_s \end{cases}, \quad (2)$$

where  $\sigma$  and  $E$  are uniaxial tensile stress and elastic modulus of component materials respectively;  $E_t$  and  $\sigma_s$  are tangent modulus and yield stress respectively. Equation (2) is used to describe the corresponding elastic-plastic stress and strain of materials in uniaxial tension.

In order to understand the uniaxial tensile mechanical properties of coatings and current collectors, a simple equation was introduced to describe the contribution of component materials to the uniaxial tensile properties of electrodes. According to Equation (1), the uniaxial tensile strains of electrodes, coatings, and current collectors are equal, and the tensile mechanical properties equations of electrode are as follows:

$$F_e = \zeta F_a + (1 - \zeta) F_c, \quad (3)$$

where  $F_e$ ,  $F_a$ , and  $F_c$  are the uniaxial tensile load of electrodes, coatings, and current collectors respectively;  $\zeta$  is the contribution coefficient of coating to uniaxial tensile load.

Since the linear response equation (Equation (3)), which describes the interactions between the coatings and the current collectors, is not entirely accurate,  $\zeta$  is, in practice, a response function that correlates with strain. Since the coating is a porous structure that contributes little to the uniaxial tensile strength of the electrodes, it was assumed that  $\zeta = 0.1$ . Figure 6a,b illustrates fitting curves for the uniaxial tensile stress-strain behaviors of the coating and current collector. The fitting curves for the coatings present that the uniaxial tensile strengths of the cathode and anode coatings are approximately 2.6 and 4 MPa, respectively. Based on peeling tests in a variety of loading directions, Zhu et al. [24] found that the adhesion strength between the coating and current collector varies between 3.0 and 4.5 MPa. They also observed that the effect of loading direction on adhesion strength is small. Therefore, the stress-strain curves of the coating and current collector that were obtained using Equations (1)–(3) satisfy the requirements of this study. The mechanical properties of the separator include nonlinear viscoelastic plasticity and anisotropy. To ensure feasibility and convergence, the mechanical properties of the separator under uniaxial tension were simplified to an elastoplastic stress-strain model (see Equation (2)), as shown in Figure 6c. The MD and TD uniaxial tensile curves were thereupon simplified. We will address the DD uniaxial tensile stress-strain relationship of the separator in a follow-up study. The mechanical properties of the component materials under uniaxial tension are presented in Table 2.

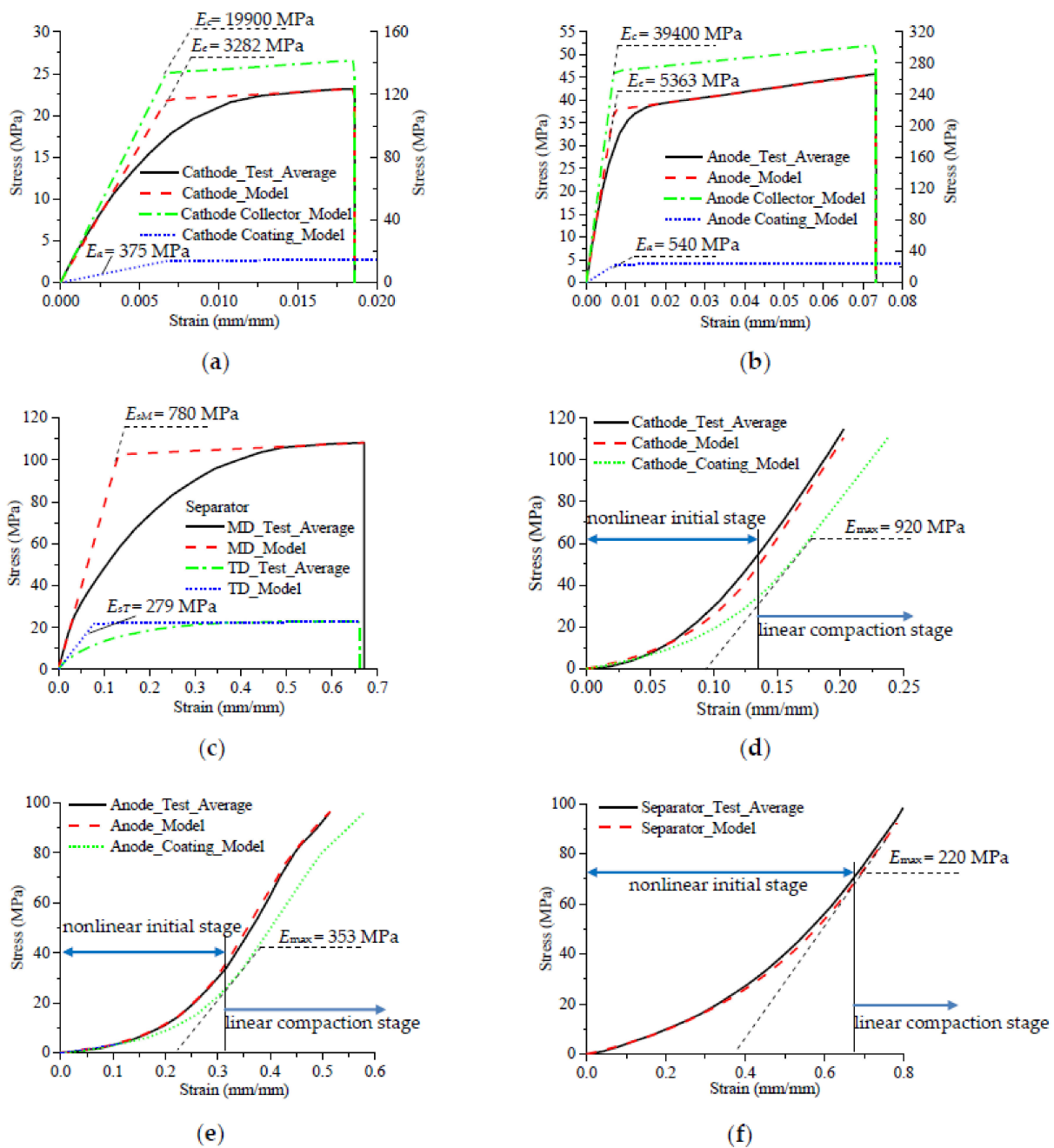


**Figure 6.** Tensile model fitting stress-strain curves: (a) Cathode/Cathode current collector/Cathode active coating; (b) Anode/Anode current collector/Anode active coating; (c) Separator; Compressive model fitting stress-strain curves: (d) Cathode/Cathode current collector/Cathode active coating; (e) Anode/Anode current collector/Anode active coating; (f) Separator.

**Table 2.** Tensile properties of lithium-ion prismatic cell components.

	Cathode		Anode		Separator
	Coating	Current Collector	Coating	Current Collector	
Elastic Modulus (MPa)	375	19,900	540	39,400	780
Yield Stress (MPa)	2.5	133	3.7	270	20
Poisson's ratio	0.01	0.33	0.01	0.343	0.2
Failure Strain	0.12 <sup>1</sup>	0.0185	0.16 <sup>1</sup>	0.073	0.67

<sup>1</sup> Reverse fitting was performed from test data collected during the local indentation test.

### 3.2. Uniaxial Compression Properties

The stress-strain curves of current collector under uniaxial tension could be used to predict their properties to uniaxial compression. The coatings, on the other hand, have strikingly different mechanical properties under tensile and compressive loads. Generally, the compression curves exhibit two distinct stages: a nonlinear initial stage, where the effective modulus stiffens gradually due to decreasing porosity, and a linear compaction stage, where the coating material has compacted fully. The gradient of the cathode specimens' stress-strain curve did not decrease even when the compressive stress was 120 MPa, which indicates that the coating and current collector have yet to yield or be damaged at this level of stress, as shown in Figure 6d. The gradient of the anode specimens' stress-strain curves begins to decrease after 80 MPa, which is caused by damage or yielding of the coating, as shown in Figure 6e. The stress-strain curves of the separator specimens under uniaxial compression are similar to those of the cathode specimens. They are initially nonlinear and transit into the linear compaction stage afterward, as shown in Figure 6f. Since the effective modulus of these materials can be divided into two stages, we have assumed that the elastic modulus,  $E$ , is equal to  $E_0$  in the initial stage and  $E_{\max}$  in the compaction stage when simulating the materials' compression response. During the stiffening process,  $E$  varies exponentially with strain,  $\varepsilon$ , as shown below:

$$E = \begin{cases} E_{\max} e^{\beta(\varepsilon - \varepsilon_p)} & \varepsilon < \varepsilon_p \\ E_{\max} & \varepsilon \geq \varepsilon_p \end{cases}, \quad (4)$$

$$E_0 = E_{\max} e^{-\beta\varepsilon_p}. \quad (5)$$

In this equation,  $\varepsilon_p$  is the plastic strain threshold for the compaction stage (i.e., the strain for the fully compacted material). If the compression strain of the material is less than  $\varepsilon_p$ ,  $E$  varies exponentially with  $\varepsilon$ ; if the strain exceeds  $\varepsilon_p$ ,  $E$  varies linearly with  $\varepsilon$ . The averaged test curves of the cathode, anode, and separator indicate that their  $\varepsilon_p$  values are 0.14, 0.32, and 0.68, respectively.  $\beta$  fits the increase in the gradient of  $E$  in relation to  $\varepsilon$  during the stiffening stage. If  $\beta$  is large, the increase in  $E$  with increasing  $\varepsilon$  will be slow. The stress-strain relationship of the component materials under compression may be subsequently obtained from Equation (4):

$$\sigma = \int_0^{\varepsilon} E d\varepsilon \begin{cases} \frac{E_{\max}(e^{\beta\varepsilon} - 1)}{\beta e^{\beta\varepsilon_p}} & \varepsilon < \varepsilon_p \\ \frac{E_{\max}(1 - e^{-\beta\varepsilon_p})}{\beta} + E_{\max}(\varepsilon - \varepsilon_p) & \varepsilon \geq \varepsilon_p \end{cases}. \quad (6)$$

Under uniaxial compression, the coating and current collector have the same external load, and the compression displacement is the sum of the two displacements. It is assumed that the uniaxial compressive stresses of electrodes, coatings, and current collectors are equal:

$$\sigma_e = \sigma_a = \sigma_c. \quad (7)$$

In Equation (6),  $\beta$  and  $E_{\max}$  are unknown.  $E_{\max}$  is derived from tests on the cathode and anode, while  $\beta$  must be determined by fitting the model against experimental data. Since the uniaxial compressive strain of the coating and current collector is equal to that of the electrode, the average strain of an electrode under uniaxial compression can be expressed as follows:

$$\bar{\varepsilon}_e = \bar{\varepsilon}_a \nu_a + \bar{\varepsilon}_c \nu_c, \quad (8)$$

where  $\bar{\varepsilon}_e$ ,  $\bar{\varepsilon}_a$  and  $\bar{\varepsilon}_c$  are the average compressive strains of electrodes, coatings, and current collectors under uniaxial compression load, respectively;  $\nu_a$  and  $\nu_c$  are the relative volume fraction of coatings and current collectors under uniaxial compression load.

Based on Equations (6)–(8), the cathode specimen has an  $E_{\max}$  of 920 MPa and  $\beta$  of 15.26, while the anode specimen has an  $E_{\max}$  of 353 MPa and  $\beta$  of 8.99. The stress-strain curves of the electrode and coating under uniaxial compression were fitted by substituting

these coefficients into Equation (6), as shown in Figure 6d,e. These results indicate that the fitting curve of the electrode is essentially identical to the average test curve. Therefore, the fitting curve of the coating is an accurate description of its mechanical properties under uniaxial compression. Figure 6f illustrates the fitted stress-strain curve of the separator under uniaxial compression, which reveals that its  $E_{\max}$  and  $\beta$  coefficients are 220 MPa and 2.64, respectively.

### 3.3. Constitutive Modeling and Simulating

The finite element models were constructed with the LS-DYNA. In the electrodes, the current collector was described with \*MAT\_003 elastoplastic material, which is suitable for isotropic hardening elements. The coatings were described with \*MAT\_026 honeycomb material, which is suitable for truly anisotropic honeycomb and foam elements. Since the separator is extremely thin and occupies a slight proportion of the electrode, it does not affect the electrodes' mechanical properties significantly. Therefore, the separator may be described using either \*MAT\_126 modified honeycomb material or \*MAT\_063 crushable foam material. Since the former is an orthogonally anisotropic honeycomb material, it is necessary to input the stress-strain curves of each of the principal directions (tension, compression, and shear). The latter is an isotropic foam material, which solely requires the input of a compressive stress-strain curve. In this study, the results obtained with both materials were compared and analyzed.

The failure modes of the cathode and anode are completely different under uniaxial tension and compression. The in-plane tensile resistance provided by the coatings is less during the tensile test, and the current collector is prone to tensile fracture. During the compression test, the contribution of the current collector to the compression load is less, and the coatings would experience a damage accumulation. Figure 2 indicates that tensile failure occurs in the following order: the cathode collector, cathode coating, anode collector, anode coating, and lastly, the separator. The coating is expected to induce a significant degree of strain localization, which will lead to deformation failure or fracture of the current collector under local indentation. The failure and crack in the current collector may directly lead to the separator failure, thereby causing short circuits in the LIB. Therefore, accurate failure criteria and failure parameters are significant for the prediction of short circuit formation in LIBs subjected to local indentation loading. The tensile failure of each component occurs at their maximum tensile strains, and the maximum tensile strains of \*MAT\_003, \*MAT\_026, and \*MAT\_126 materials are presented in Table 2. As for the failure under compression, the damage behaviors of \*MAT\_026 and \*MAT\_063 materials were implemented by inputting their stress-strain curves under uniaxial compression. \*MAT\_126 material not only requires MD- and TD-uniaxial tension stress-strain curves (see Figure 6c), a uniaxial compression curve (see Figure 6f), but also requires to use the stress transformation equations of composite materials to obtain the stress-strain curve for DD shear. Figure 7a illustrates the relationship between two coordinate systems in the separator plane, where  $\theta$  represents the anticlockwise angle between the 12-coordinate system and XY-coordinate system. The stress equilibrium equation can be derived from the inter-element equilibrium conditions of the oblique plane (see Figure 7b):

$$\begin{bmatrix} \sigma_1 \\ \sigma_2 \\ \tau_{12} \end{bmatrix} = \begin{bmatrix} \cos^2 \theta & \sin^2 \theta & -2 \sin \theta \cos \theta \\ \sin^2 \theta & \cos^2 \theta & 2 \sin \theta \cos \theta \\ \sin \theta \cos \theta & -\sin \theta \cos \theta & \cos^2 \theta - \sin^2 \theta \end{bmatrix} \begin{bmatrix} \sigma_x \\ \sigma_y \\ \tau_{xy} \end{bmatrix}, \quad (9)$$

where,  $\sigma_1$  and  $\sigma_2$  are the MD- and TD-uniaxial tensile stresses of the separators, respectively;  $\sigma_x$  and  $\sigma_y$  are the stress components of  $\theta$  angle in the MD and TD counter clockwise rotation respectively;  $\tau_{12}$  is the shear stress in the 12-coordinate system;  $\tau_{xy}$  is the shear stress in the XY-coordinate system.

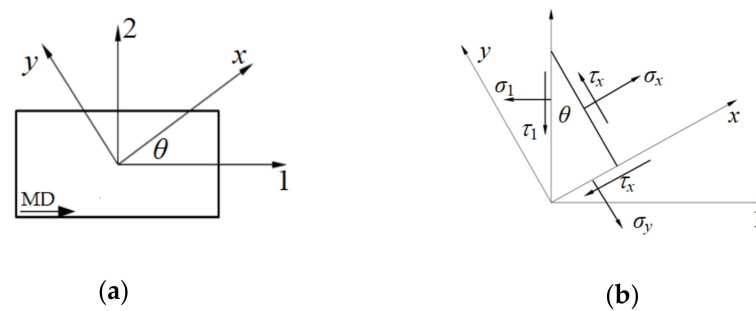


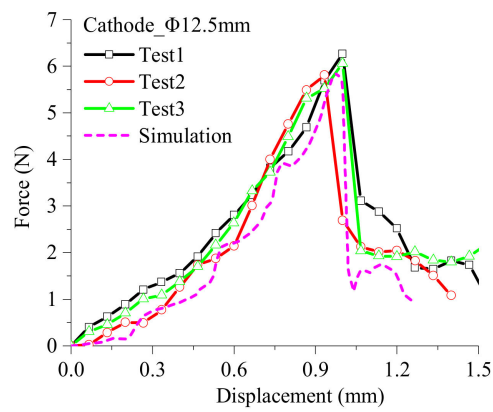
**Figure 7.** Diagram of separator plane coordinate system: (a) Rotating coordinate system in the separator plane; (b) Equilibrium coordinate system in oblique plane.

Assuming that  $\theta = 45^\circ$  and  $\sigma_1$ ,  $\sigma_2$  and  $\sigma_x$  are the MD-, TD-, and DD-uniaxial average tensile stresses of the separator in Figure 2f, respectively; According to Equation (10), the shear stress expression of separator in the DD can be obtained:

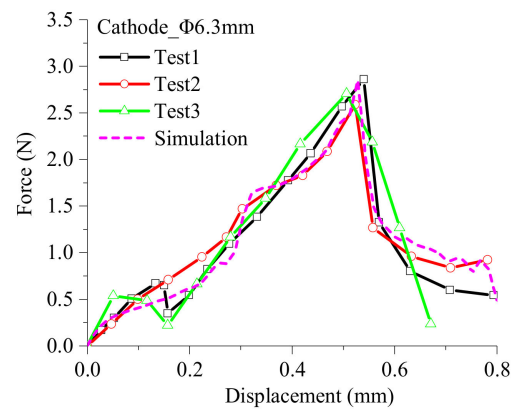
$$\tau_{12} = \sigma_x - \frac{(\sigma_1 + \sigma_2)}{2}. \quad (10)$$

\*MAT\_063 material requires solely the input of a compressive stress-strain curve, and the tension cut-off stress was defined as the average flow stress for tension in the MD, 108 MPa. Finite element models for the cathode, anode, and separator were constructed. The spherical punches were represented as rigid spheres with diameters of  $\Phi 12.5$  and  $\Phi 6.3$  mm. The contact between the spherical punch and component material model was defined as an automatic surface-to-surface contact with a friction coefficient of 0.4. The size of the smallest element was 0.1 mm in the contact zone and 0.8 mm in the noncontact zone. All of the component material models consisted of solid elements, whereas the spherical punches were made of shell elements. The coatings were connected to the current collector via common nodes. The coating and separator had a minimum two solid elements through their thickness. The maximum tensile strain criterion was varied for each component material model, and \*MAT\_ADD\_EROSION was used to delete the elements that reached their corresponding maximum tensile strain value. This ensured that the numerical simulation would not diverge on account of excessively large deformations.

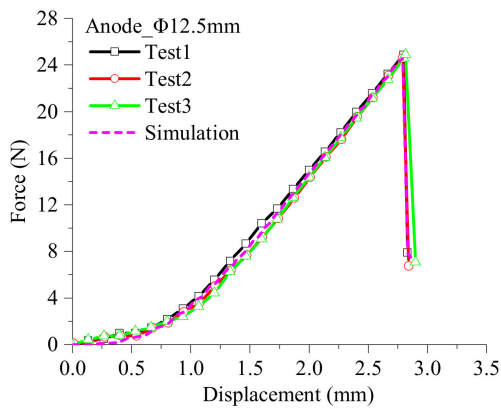
Figure 8a–d reveals that the experimental curves of the spherical indentation tests on the anode/cathode were accurately predicted by our numerical simulations. However, the simulation of the anode being indented by a  $\Phi 6.3$  mm spherical punch exhibited slightly higher load intensities than the experiment. Figure 8e,f, on the other hand, indicates that the simulated curves for spherical indentation tests on the separator are significantly different from the experimental curves. This could be attributed to the use of simplified material models to describe the separator. It is found that the strength of the \*MAT\_126 model is significantly higher than the \*MAT\_063 model, and provides a more accurate approximation of the separator's mechanical behaviors, but the calculation time is also longer. The elements that failed during the simulated spherical indentation test with a  $\Phi 12.5$ -mm spherical punch were deleted from the cathode, anode, and separator models, as shown in Figure 9. The simulated cracks in the cathode and anode models are similar to the experimentally observed cracks. In the \*MAT\_126 separator model, the cracks are slightly different from the experiment, but the crack initiation position and primary shear band are similar to those of the experiment. However, the cracks in \*MAT\_063 separator model are essentially different from those in the experiment (not shown). By comparing the simulated and experimental results of the local indentation tests, we have proved that the abovementioned models are capable of predicting the macroscopic force-displacement curves and mesoscopic failure modes of a prismatic LIB's component materials.



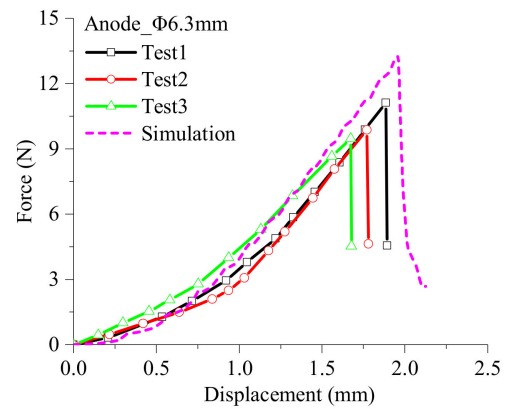
(a)



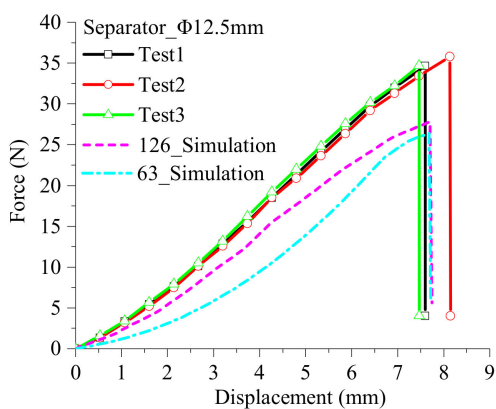
(b)



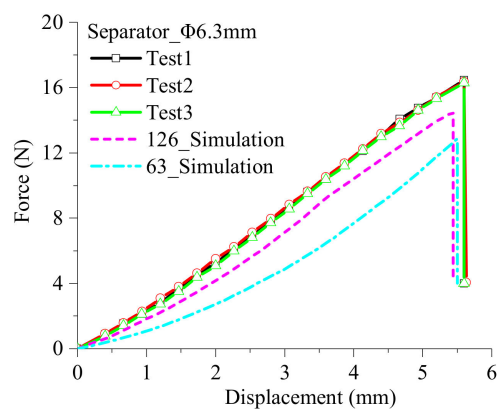
(c)



(d)



(e)



(f)

**Figure 8.** Force-displacement curves of lithium-ion prismatic cell components under different sizes of spherical punches: (a) Cathode tests and simulation under  $\Phi 12.5$  mm; (b) Cathode tests and simulation under  $\Phi 6.3$  mm; (c) Anode tests and simulation under  $\Phi 12.5$  mm; (d) Anode tests and simulation under  $\Phi 6.3$  mm; (e) Separator tests and simulation under  $\Phi 12.5$  mm; (f) Separator tests and simulation under  $\Phi 6.3$  mm.

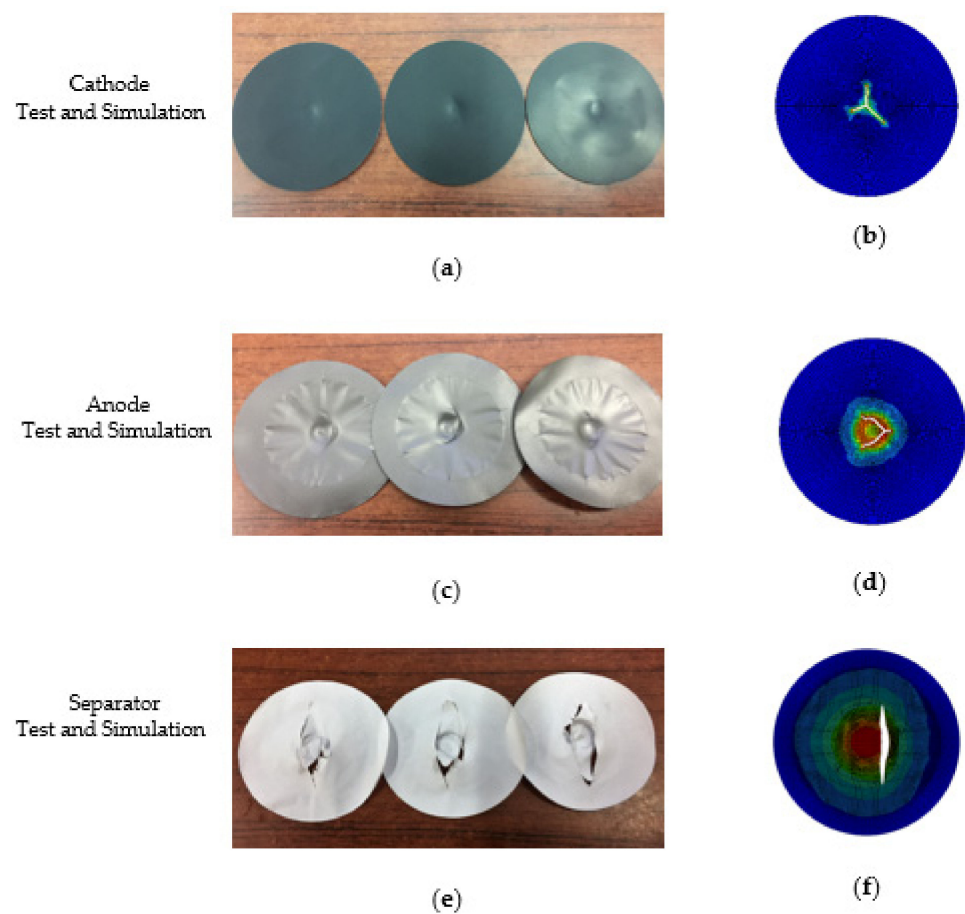


**Figure 9.** Failure mode of lithium-ion prismatic cell components under spherical punch: (a) Cathode test results; (b) Cathode simulation results; (c) Anode test results; (d) Anode simulation results; (e) Separator test results; (f) Separator simulation results.

#### 4. Progressive Failure of Cathodes and Anodes

In order to further understand the failure mechanisms of lithium-ion prismatic cell under spherical indentation, it is necessary to understand the progressive deformation failure of the cell interior. Considering that the interior is composed of component materials stacked alternately, a layer element model (LEM) composed of separator, cathode, separator, and anode is established. The mechanical behavior and failure response of LEM were studied under spherical indentation. The simulation results were compared and verified with the experimental results. Based on the LEM, a discrete layered structure model was constructed to analyze the progressive failure mechanisms of cathodes and anodes under spherical punch.

##### 4.1. Modeling of Mesosstructural Layer Element

The specimen dimensions and experimental apparatus are the same as those in Figure 4. The  $\Phi 6.3$  mm and  $\Phi 25$  mm spherical punches were used to perform quasi-static local indentation at a loading speed of 1 mm/min (see Figure 10a). We chose to use a  $\Phi 25$  mm spherical punch because of the universal applicability of this loading condition. The finite element models for the cathode, anode, and separator were already constructed in the previous section. The surfaces were modeled using CONTACT\_AUTOMATIC\_SURFACE\_TO\_SURFACE protocol to prevent the elements of the cathode, anode, and separator from penetrating each other. The kinetic friction coefficient was set to 0.4. Figure 10b illustrates the stacked separator-cathode-separator-cathode model; this is the repeating element that makes up the internal configuration of a prismatic LIB, the LEM. The finite element model of a  $\Phi 6.3$ -mm spherical punch acting on the LEM

is depicted in Figure 10c. The sizes of the elements in the contact zone and noncontact zone were 0.1 and 0.6 mm, respectively, and there were 202,268 nodes and 160,758 elements in the LEM. The separator was represented either by \*MAT\_126 material or by \*MAT\_063 material.

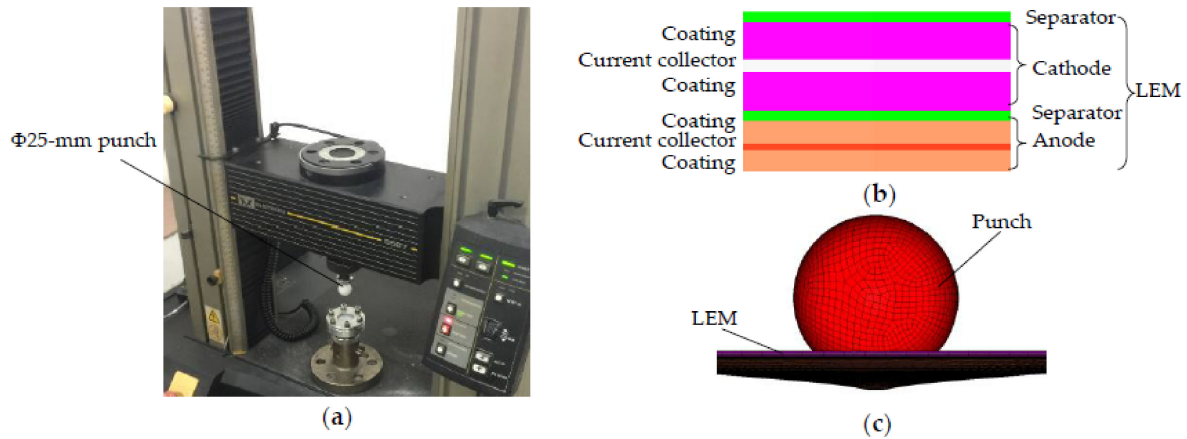


**Figure 10.** Test and simulation of an layer element model (LEM) under spherical punch: (a) Experimental setup; (b) A layer element structure model; (c) Finite element model of a layer element.

The simulated and experimental results for spherical indentation with  $\Phi 6.3$  mm and  $\Phi 25$  mm spherical punches are illustrated in Figure 11. Although the simulated and experimental peak forces and failure displacements are slightly different, the simulated and experimental curves are essentially the same from the initial stage (initial stiffening) up to the failure-induced load drop-offs. Furthermore, there were no significant differences between the results obtained with \*MAT\_126 or \*MAT\_063 to represent the separators. This indicates that the separator influences a prismatic LIB's mechanical properties minimally. Since the use of the \*MAT\_126 material is computationally expensive and the failure modes of the separator are not important for this study, \*MAT\_063 material was used for the separator in all subsequent simulations to improve computational efficiency. Spherical indentation leads to complex mechanical behaviors in the layer elements since this includes tensile failures in the current collector, compressive damage in the coatings, and the formation of holes owing to debonding between the coatings and current collectors. There are two distinct force drop in the force-displacement curve of a layer element. The first force drop is caused by the tensile failure of the cathode current collector; further increase in load will eventually lead to the second force drop, which is caused by the tensile failure of the anode current collector. By analyzing the results, it was found that the cathode current collector would fail first, followed by the anode current collector and, finally, the separators. Therefore, strain localization in the coating does not lead directly to short circuits in a prismatic LIB since short circuits are primarily caused by separator damage owing to fractures and slips in the current collectors.

According to Figure 11a, the cathode current collector cracked when the strain reached 0.31 (displacement = 0.87 mm) during the indentation by a  $\Phi 6.3$  mm spherical punch. This failure manifested itself as a cross-shaped crack in the contact zone, and the force drops off when the crack propagates to the coating on the current collector. When the strain increases to 0.86 (displacement = 1.83 mm), the anode current collector begins to exhibit tensile fractures, which appear as cross-shaped cracks in the contact zone. Afterward, the force drops off again when these fractures extend to the coating. After the cathode and anode in the layer element have cracked and failed, the separator will continue to bear loads until it fails. To simulate a universally applicable loading condition, a layer element was indented by a  $\Phi 25$  mm spherical punch, as shown in Figure 11b. The simulated curve agrees well with the experimental curve, and the stiffening response was essentially identical in both curves. However, the simulated peak force and failure displacement are slightly higher



than those of the experimental curve. During the simulation, crack initiation occurred just off the center of the spherical punch, and the fracture eventually propagates to form a petal-shaped crack, similar to that in the experiment.

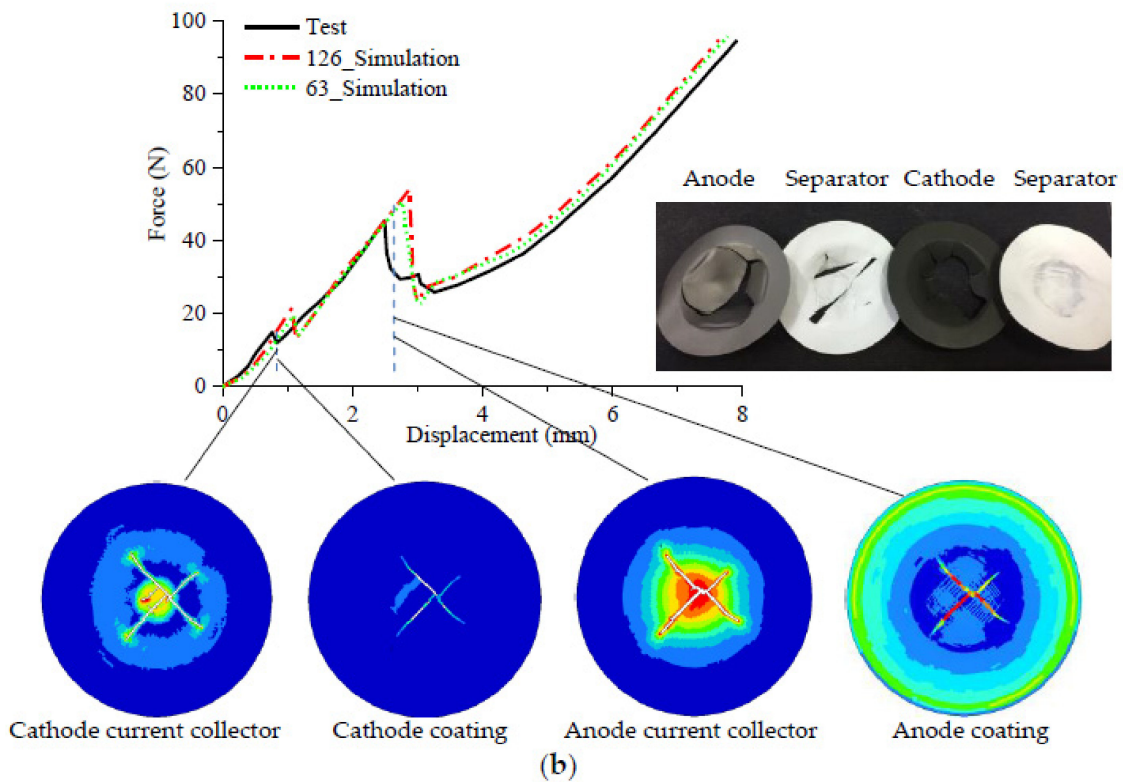
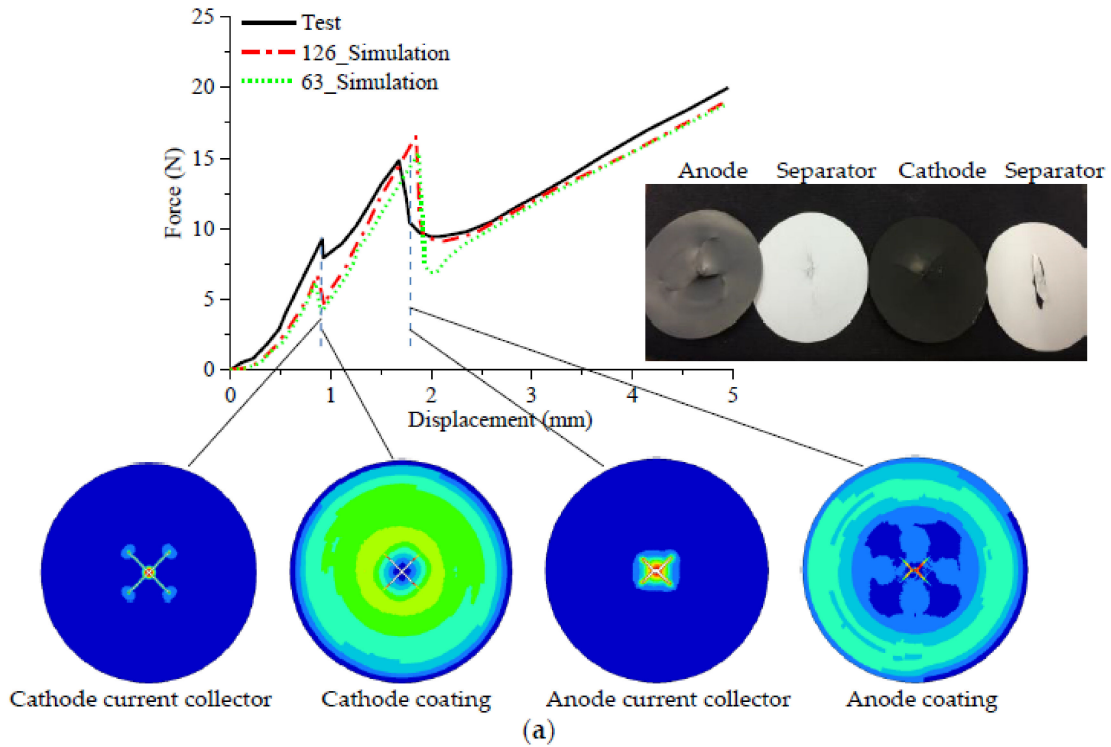


**Figure 11.** Force-displacement curves of a layer element under spherical punch: (a) Comparison of test and simulation curves under  $\Phi 6.3$ -mm spherical punch; (b) Comparison of test and simulation curves under  $\Phi 25$  mm spherical punch.

#### 4.2. Progressive Failure of Cathodes and Anodes on Multilayered LEMs

The results above revealed that a layer element would fail in a progressive manner under local indentation. As the basic element of the interior, the layer element determines the mechanical behavior and deformation failure of the cell interior. Considering that the layer element number of the lithium-ion prismatic cell is up to 45 layers, it needs to be simplified. Figure 12a illustrates a local indentation test on a stack of layer elements. Based on this, to ensure that the model would be computationally feasible, we constructed a 1/4 finite element model of an eight-layer layer element stack to simulate their inter-component interactions and failure propagation mechanisms. An axially symmetrical model of a  $\Phi 6.3$  mm spherical punch acting on a multilayered stack of layer elements is depicted in Figure 12b. The spherical punch was a rigid sphere moving in the through-thickness direction of the LEM, and the base was a completely constrained rigid plane. To prevent the elements of the spherical punch, cathode, anode, separator, and rigid plane from penetrating each other, the surfaces were modeled with the CONTACT\_AUTOMATIC\_SURFACE\_TO\_SURFACE protocol, with a kinetic friction coefficient of 0.4. The sizes of the smallest elements in the contact zone and noncontact zone were 0.1 and 0.6 mm, respectively, and the model contained 502,418 nodes and 380,800 elements (see Figure 12c). This simulation required 23 h to complete with 44 CPUs.

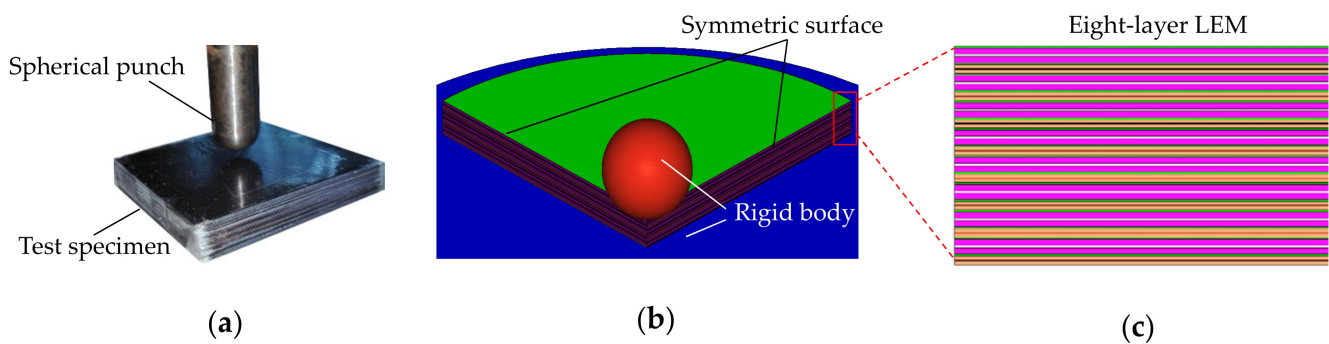


**Figure 12.** Local indentation test of multilayered LEMs under 6.3 mm spherical punch: (a) Experimental setup; (b) Finite element model of multilayered LEMs; (c) Enlarged view of layered structure of finite element model.

Figure 13 compares the simulated and experimental force-displacement curves of the anodes in the eight-layer LEM. The force-displacement curve of the anodes indicates that ring-shaped cracks formed in the first anode current collector layer when the strain due to spherical indentation reached 0.57 (displacement = 0.94 mm). The crack in the anode current collector led to local stress concentrations, which caused the damage to propagate to its coating rapidly. The damage on the coating manifested itself as elements being deleted in the contact zone around the indenter, and it could be observed that the deleted elements formed ring-shaped cracks. As damage continued to accumulate during the indentation test, a rough ring-shaped section was formed by the failure cracks of the first anode layer. In addition, the ruptured areas on the top and bottom side of the coating were almost identical. Figure 14 compares the experimental and simulated failure modes of the eight-layer model's anode layers. Here, it is obvious that failures in the first, second, and third anode layers led to a variety of failure modes via the propagation of failure cracks from one layer to another. The failure mode of the first layer was a distinct ring-shaped crack, which had a significantly larger ruptured area and smoother crack edges than the failure mode in the second layer. In the third anode layer, element deletion was not observed. This is close to the experimental test of the third anode layer, which exhibited solely fine cracks at the center of the contact zone.

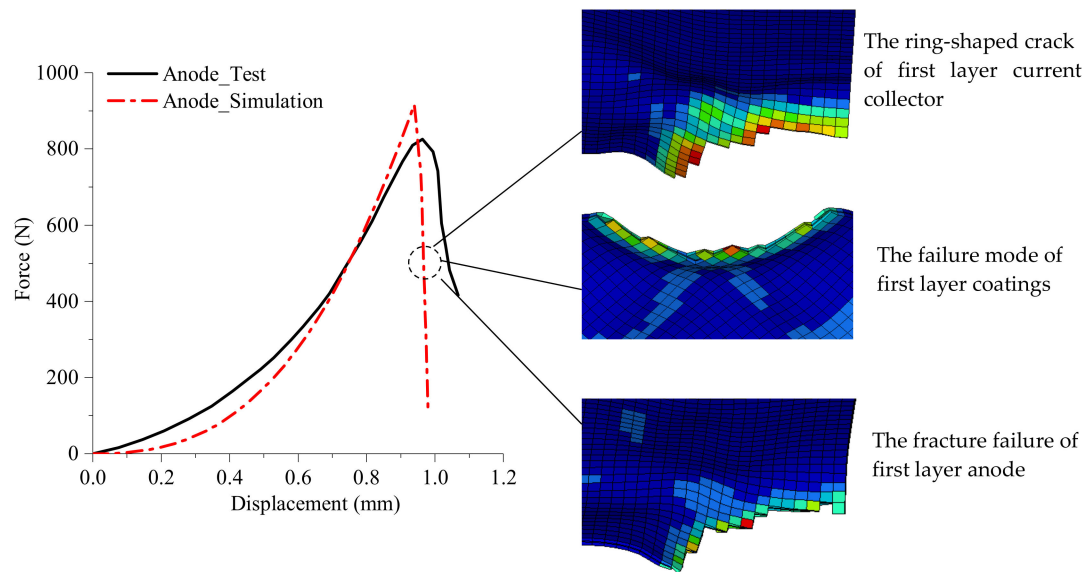


**Figure 13.** Comparison of experimental and simulated force-displacement curve and numerically prediction failure evolution of anode in multilayered LEMs during local indentation.

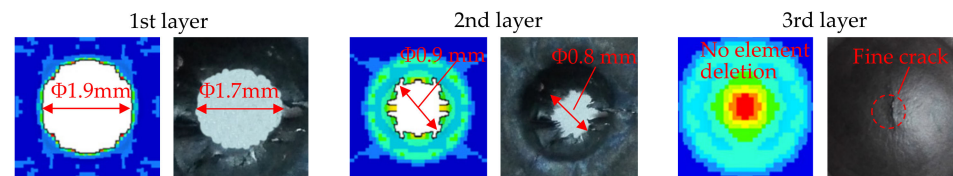


**Figure 14.** Comparison between experimental tests and simulation of fracture modes of anodes across different layers under local indentation.

The tensile failure strain of the cathode current collector was relatively low, as shown in Figure 15. When the strain due to indentation loading increased to 0.21 (displacement = 0.36 mm), the cathode current collector failed at the center of the contact zone and the cracks propagated along its symmetric edges. The damage of the cathode coating began when the strain increased to 0.26 (displacement = 0.43 mm); this damage manifested itself as compression fractures in the contact zone and tensile fractures that propagated along the symmetric edges. The strain's increase to 0.33 (displacement = 0.54 mm) caused the compression fracture in the first cathode layer to propagate in the annular direction from the center of the contact zone while tensile cracks continued to propagate along the symmetric edges, thereby forming a petal-like crack. The tensile strain-induced changes of the first, second, and third cathode layers as well as their top and bottom coatings are shown in Figure 16a. It is clear that the tensile strain on the bottom coating is much higher than that on the top coating, which implies that the bottom coating will fail first. By comparing the simulated and experimental results, it becomes clear that the failure behaviors of the cathode and anode under spherical indentation are radically different. In the first cathode layer, the number of elements that were deleted from the bottom coating is significantly higher than that from the top coating, and the failure modes of the bottom coating are somewhat reminiscent of the anode's failure modes. In the second cathode layer, the outer elements around the center of the contact zone were deleted; this resembles the ring-shaped cracks that were experimentally observed in the contact zone, as shown in Figure 16b. The analysis above indicates that the failure responses of the cathode and anode to spherical indentation are somewhat different. These differences may be due to differences in strength between the current collectors and coatings, or to differences in the constitutive properties of the cathode and anode coatings materials.

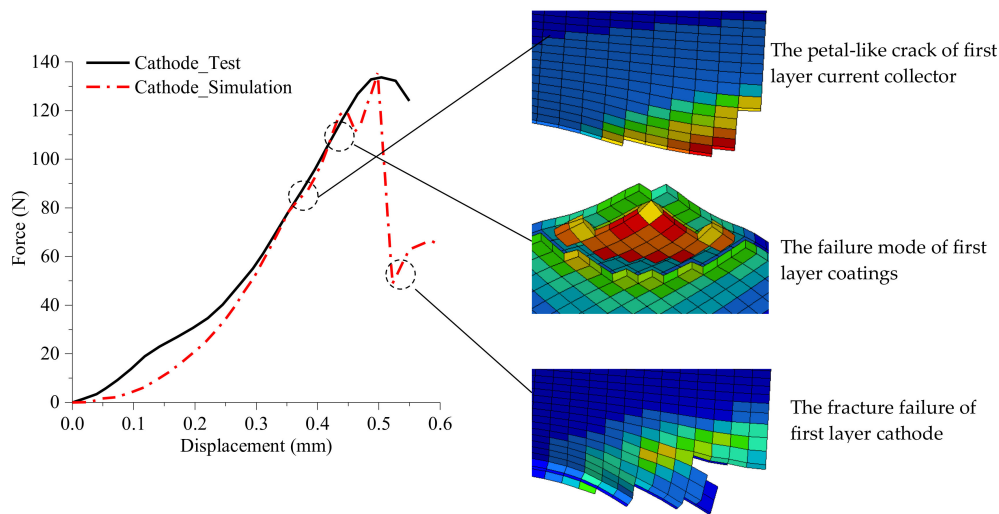


**Figure 15.** Comparison of experimental and simulated force-displacement curve and numerically prediction failure evolution of cathode in multilayered LEMs during local indentation.

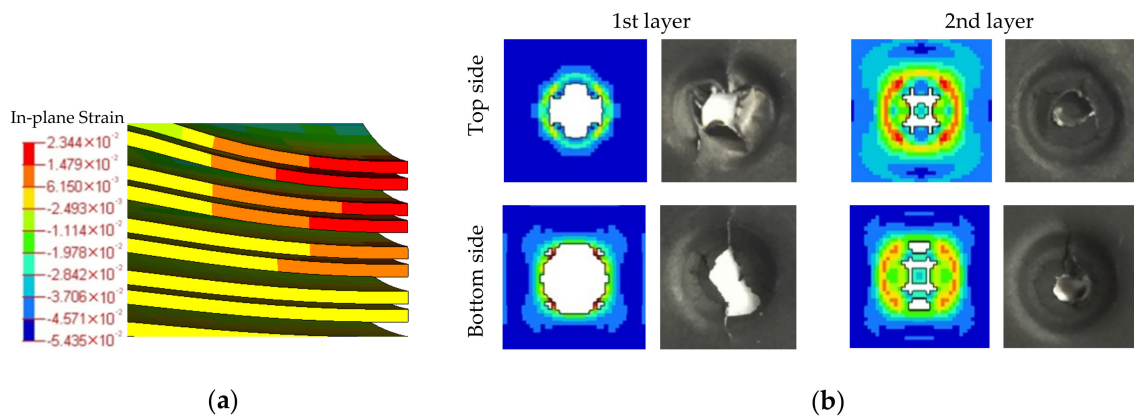


**Figure 16.** Simulation analysis of cathode: (a) The numerically prediction in-plane strain contour of the cathode coatings show that the cathode coatings on the lower side of the cathode current collector produces higher in-plane tensile strains than the layer immediately above the cathode current collector; (b) Comparison between experimental tests and simulation of fracture modes of cathodes across different layers under local indentation.

According to the local indentation results in the eight-layer LEM, the electrode materials of the lithium-ion prismatic cell produce progressive failure, that is to say, the failure of the cell interior is a propagation from the local fracture to the overall failure. The fracture of current collectors and strain localization of coating materials cannot be distinguished by macroscopic force-displacement response curve, because the whole failure process is instantaneous. The multilayered LEMs can reasonably predict the failure modes and understand the progressive failure mechanisms of component materials. In addition, during the local indentation, the strain localization of the coating materials of the electrodes lead to the rapid increase in the current collectors' equivalent strain, which ultimately causes the current collectors to crack. Therefore, internal short circuits are primarily caused by separator damage owing to fractures and slips in the current collectors.

## 5. Conclusions

The mechanical failure behavior of prismatic LIB component materials were expressed experimentally and numerically. The mechanical properties of the anode, cathode and separator under uniaxial tension, compression, and biaxial indentation were tested, and the results of these tests were used to derive the stress-strain constitutive models of the metallic current collectors, active coatings, and separator. The maximum tensile strain

failure criterion was proposed to describe the indentation failure of component materials, and an ultrathin LEM was constructed by the experimental stress-strain curves to simulate the mechanical behaviors and failure modes under the spherical punches. Through the combination of experiments and numerical simulations, we identified the progressive failure mechanisms of the n-layer LEM stacked structure model, including the tensile and compressive failure of cathodes and anodes, and compared the failure modes of experimental tests and simulations.

Based on the numerical simulations of the LEM, it was determined that failure cracks in the current collectors could rupture their adjacent separators, which ultimately led to internal short circuit. By constructing an accurate layered structure model, we were able to accurately predict the force-displacement relationships, failure modes, and the moment of short circuit initiation in a prismatic LIB. These predictions will provide a profound insight into the progressive failure mechanisms of prismatic LIBs subjected to mechanical load. Furthermore, we demonstrated that the macroscopic force-displacement curve of a LEM had no significant relationship with the use of different types of material models to represent the separators. The anisotropic material model could characterize the mechanical behaviors and failure modes of the separator more accurately, but it would consume more calculation time. In the layered structure model, if the failure modes of the separator are not important, the isotropic material model could be used to represent the separator to reduce the calculation time.

**Author Contributions:** Conceptualization, Z.L., J.C. and F.L.; methodology, Z.L.; software, Z.L.; validation, Z.L., J.C. and F.L.; formal analysis, Z.L.; investigation, Z.L.; resources, F.L.; data curation, Z.L. and Y.L.; writing—original draft preparation, Z.L.; writing—review and editing, Z.L.; visualization, Z.L.; supervision, J.C.; project administration, J.C. and F.L.; funding acquisition, J.C. and F.L. All authors have read and agreed to the published version of the manuscript.

**Funding:** This research was funded by the National Key Research and Development Program of China, grant number 2018YFB0104100.

**Institutional Review Board Statement:** The study did not involve humans or animals.

**Informed Consent Statement:** The study did not involve humans.

**Data Availability Statement:** The study did not report any data.

**Acknowledgments:** This work was supported by the National Key Research and Development Program of China (2018YFB0104100).

**Conflicts of Interest:** The authors declare no conflict of interest. The funders had no role in the design of the study; in the collection, analyses, or interpretation of data; in the writing of the manuscript, or in the decision to publish the results.

## Abbreviations

LIBs	lithium-ion batteries
LEM	layer element model
RVEs	representative volume elements
ASTM	American society of testing materials
$\varepsilon_e, \varepsilon_a, \varepsilon_c$	Uniaxial tensile strains of electrode, coating, current collector
$\sigma_s$	Yield stress
$E_t$	Tangent modulus
$F_e, F_a, F_c$	Uniaxial tensile load of electrode, coating, current collector
$\xi$	Contribution coefficient of coating to tensile load
$E_0$	Initial modulus
$E_{\max}$	Compaction modulus
$\beta$	Fitting coefficient
$\sigma_e, \sigma_a, \sigma_c$	Uniaxial compressive stress of electrode, coating, current collector
$\bar{\varepsilon}_e, \bar{\varepsilon}_a, \bar{\varepsilon}_c$	Average compressive strain of electrode, coating, current collector
$v_a, v_c$	Relative volume fraction of coating, current collector

## References

1. Kermani, G.; Sahraei, E. Review: Characterization and Modeling of the Mechanical Properties of Lithium-Ion Batteries. *Energies* **2017**, *10*, 1730. [[CrossRef](#)]
2. Xia, Y.; Li, T.; Ren, F.; Gao, Y.; Wang, H. Failure analysis of pinch-torsion tests as a thermal runaway risk evaluation method of Li-ion cells. *J. Power Sources* **2014**, *265*, 356–362. [[CrossRef](#)]
3. Zhang, X.; Sahraei, E.; Wang, K. Li-ion Battery Separators, Mechanical Integrity and Failure Mechanisms Leading to Soft and Hard Internal Shorts. *Sci. Rep.* **2016**, *6*, 32578. [[CrossRef](#)]
4. Cannarella, J.; Arnold, C.B. Stress evolution and capacity fade in constrained lithium-ion pouch cells. *J. Power Sources* **2014**, *245*, 745–751. [[CrossRef](#)]
5. Cannarella, J.; Arnold, C.B. State of health and charge measurements in lithium-ion batteries using mechanical stress. *J. Power Sources* **2014**, *269*, 7–14. [[CrossRef](#)]
6. Zhou, W.; Hao, F.; Fang, D. The effects of elastic stiffening on the evolution of the stress field within a spherical electrode particle of lithium-ion batteries. *Int. J. Appl. Mech.* **2013**, *5*, 1350040. [[CrossRef](#)]
7. Zhou, W. Effects of external mechanical loading on stress generation during lithiation in Li-ion battery electrodes. *Electrochim. Acta* **2015**, *185*, 28–33. [[CrossRef](#)]
8. Marcicki, J.; Bartlett, A.; Yang, X.G.; Mejia, V.; Zhu, M.; Chen, Y. Battery Abuse Case Study Analysis Using LS-DYNA. In Proceedings of the 14th International LS-DYNA Users Conference, Dearborn, MI, USA, 12–14 June 2016.
9. Wang, H.; Kumar, A.; Simunovic, S.; Allu, S.; Kalnaus, S.; Turner, J.A.; Helmers, J.C.; Rules, E.T.; Winchester, C.S.; Gorney, P. Progressive mechanical indentation of large-format Li-ion cells. *J. Power Sources* **2017**, *341*, 156–164. [[CrossRef](#)]
10. Finegan, D.; Tjaden, B.; Heenan, T.M.; Jervis, R.; Michiel, M.D.; Rack, A.; Hinds, G.; Brett, D.J.; Shearing, P.R. Tracking Internal Temperature and Structural Dynamics during Nail Penetration of Lithium-Ion Cells. *J. Electrochem. Soc.* **2017**, *164*, 3285–3291. [[CrossRef](#)]
11. Sahraei, E.; Hill, R.; Wierzbicki, T. Calibration and finite element simulation of pouch lithium-ion batteries for mechanical integrity. *J. Power Sources* **2012**, *201*, 307–321. [[CrossRef](#)]
12. Sahraei, E.; Campbell, J.; Wierzbicki, T. Modeling and short circuit detection of 18650 Li-ion cells under mechanical abuse conditions. *J. Power Sources* **2012**, *220*, 360–372. [[CrossRef](#)]
13. Greve, L.; Fehrenbach, C. Mechanical testing and macro-mechanical finite element simulation of the deformation, fracture, and short circuit initiation of cylindrical Lithium ion battery cells. *J. Power Sources* **2012**, *214*, 377–385. [[CrossRef](#)]
14. Wang, H.; Simunovic, S.; Maleki, H.; Howard, J.N.; Hallmark, J.A. Internal configuration of prismatic lithium-ion cells at the onset of mechanically induced short circuit. *J. Power Sources* **2016**, *306*, 424–430. [[CrossRef](#)]
15. Chung, S.H.; Tancogne-Dejean, T.; Zhu, J.; Luo, H.; Wierzbicki, T. Failure in lithium-ion batteries under transverse indentation loading. *J. Power Sources* **2018**, *389*, 148–159. [[CrossRef](#)]
16. Sheidaei, A.; Xiao, X.; Huang, X.; Hitt, J. Mechanical behavior of a battery separator in electrolyte solutions. *J. Power Sources* **2011**, *196*, 8728–8734. [[CrossRef](#)]
17. Lee, H.; Yanilmaz, M.; Topralci, O.; Fu, K.; Zhang, X. A review of recent developments in membrane separators for rechargeable lithium-ion batteries. *Energy Environ. Sci.* **2014**, *7*, 3857–3886. [[CrossRef](#)]
18. Zhang, C.; Santhanagopalan, S.; Sprague, M.A.; Pesaran, A.A. Coupled mechanical-electrical-thermal modeling for short-circuit prediction in a lithium-ion cell under mechanical abuse. *J. Power Sources* **2015**, *290*, 102–113. [[CrossRef](#)]
19. Zhang, C.; Xu, J.; Cao, L.; Wu, Z.; Santhanagopalan, S. Constitutive behavior and progressive mechanical failure of electrodes in lithium-ion batteries. *J. Power Sources* **2017**, *357*, 126–137. [[CrossRef](#)]
20. Sahraei, E.; Bosco, E.; Dixon, B.; Lai, B. Microscale failure mechanisms leading to internal short circuit in Li-ion batteries under complex loading scenarios. *J. Power Sources* **2016**, *319*, 56–65. [[CrossRef](#)]
21. Zhang, X.; Sahraei, E.; Wang, K. Deformation and failure characteristics of four types of lithium-ion battery separators. *J. Power Sources* **2016**, *327*, 693–701. [[CrossRef](#)]
22. Sahraei, E.; Meier, J.; Wierzbicki, T. Characterizing and modeling mechanical properties and onset of short circuit for three types of lithium-ion pouch cells. *J. Power Sources* **2014**, *247*, 503–516. [[CrossRef](#)]
23. Wierzbicki, T.; Sahraei, E. Homogenized mechanical properties for the jellyroll of cylindrical Lithium-ion cells. *J. Power Sources* **2013**, *241*, 467–476. [[CrossRef](#)]
24. Zhu, J.; Li, W.; Wierzbicki, T.; Xia, Y.; Harding, J. Deformation and failure of lithium-ion batteries treated as a discrete layered structure. *Int. J. Plasticity* **2019**, *121*, 293–311. [[CrossRef](#)]
25. Wang, H.; Watkins, T.R.; Simunovic, S.; Bingham, P.R.; Allu, S.; Turner, J.A. Fragmentation of copper current collectors in Li-ion batteries during spherical indentation. *J. Power Sources* **2017**, *364*, 432–436. [[CrossRef](#)]